



Contents lists available at ScienceDirect

## Journal of Alloys and Compounds

journal homepage: <http://www.elsevier.com/locate/jalcom>

## Lattice dynamics of thermoelectric palladium sulfide

Liu-Cheng Chen<sup>a, b, c</sup>, Qing Peng<sup>d</sup>, Hao Yu<sup>c</sup>, Hong-Jie Pang<sup>c</sup>, Bin-Bin Jiang<sup>e, f</sup>, Lei Su<sup>g</sup>, Xun Shi<sup>e</sup>, Li-Dong Chen<sup>e</sup>, Xiao-Jia Chen<sup>c, \*</sup>

HPSTAR  
750-2019

<sup>a</sup> Key Laboratory of Materials Physics, Institute of Solid State Physics, Chinese Academy of Sciences, Hefei 230031, China<sup>b</sup> University of Science and Technology of China, Hefei 230026, China<sup>c</sup> Center for High Pressure Science and Technology Advanced Research, Shanghai 201203, China<sup>d</sup> Department of Nuclear Engineering and Radiological Science, University of Michigan, Ann Arbor, MI, 48109, USA<sup>e</sup> State Key Laboratory of High Performance Ceramics and Superfine Microstructure, Shanghai Institute of Ceramics, Chinese Academy of Science, Shanghai 200050, China<sup>f</sup> University of Chinese Academy of Sciences, Beijing 100049, China<sup>g</sup> Key Laboratory of Photochemistry, Institute of Chemistry, Chinese Academy of Sciences, Beijing 100080, China

## ARTICLE INFO

## Article history:

Received 25 March 2019

Received in revised form

21 May 2019

Accepted 23 May 2019

Available online 26 May 2019

## Keywords:

Palladium sulfide

X-ray diffraction

Raman spectra

Ab initio calculations

## ABSTRACT

Highly efficient thermoelectric materials always have low thermal conductivities. Their phonon spectrum information is essential for understanding the procedure of thermal transport on thermoelectrics. Recently, palladium sulfide was found to be a potential thermoelectric material. However, the high thermal conductivity limits its thermoelectric performance and technological applications. Here, the phonon dispersion and phonon density of state in PdS are presented by using the first-principles theory. The phonon modes are assigned and compared with experiments. The evolution of optical modes with pressure is studied by using Raman spectroscopy. The low-energy and high-energy phonon bands are related to the vibrations of the heavy atom and the light atom, respectively. By combining Raman scattering and X-ray diffraction measurements, we obtain the mode-Grüneisen parameters for the detected phonon modes. The small mode-Grüneisen parameters indicate a weak anharmonicity in this material. This offers an explanation for its high thermal conductivity. The evolution of linewidths with pressure accounts for the decrease of the thermal conductivity upon compression.

© 2019 Elsevier B.V. All rights reserved.

## 1. Introduction

Currently, the world is facing numerous challenges relating to energy supply and environment consumption. High-efficiency thermoelectric materials, which can directly convert waste heat into electric power without producing unusable heat, possess great potential to settle these conditions. The dimensionless figure of merit ( $zT$ ), which can be expressed as  $zT = S^2 T \sigma \kappa^{-1}$ , where  $S$  is the Seebeck coefficient,  $\sigma$  is the electrical conductivity,  $T$  is the absolute temperature, and  $\kappa$  is the thermal conductivity, determines the maximum efficiency of the conversion process. This formula expresses the fact that large  $S$ , high  $\sigma$ , and low  $\kappa$  will be need for a high efficiency [1–3]. In fact, the produced electrical energy is in the form of current which is driven by thermoelectric voltage. Meanwhile, considering the parasitic relationship between heat

conduction and electrical resistance, it is obvious that efficient thermoelectric materials always have low thermal conductivities [4–6]. Palladium sulfide (PdS), which belongs to transition metal sulfides with an ideal band gap of 1.6 eV, has many potential applications in semiconducting, photoelectrochemical and photovoltaic fields [7–9]. In addition, it also presented many potential device applications in catalysis and acid resistant and high temperature electrodes [10,11]. Surprisingly, PdS also presents superconducting properties under pressure [12]. As a potential thermoelectric, it possesses intrinsic large power factors of  $27 \mu\text{Wcm}^{-1}\text{K}^{-2}$  and a moderate  $zT$  value around 800 K. The relative high thermal conductivity ( $24 \text{Wm}^{-1}\text{K}^{-1}$ ) is the main factor for limiting its thermoelectric performance [13,14]. Thus, if the large thermal conductivity could be suppressed while keeping the good electrical properties, PdS will be a good candidate for thermoelectric applications.

Due to the crucial role of phonon information for understanding the thermal transport properties in thermoelectric materials, it is necessary to analysis the phonon dispersion and other related

\* Corresponding author.

E-mail address: [xjchen@hpstar.ac.cn](mailto:xjchen@hpstar.ac.cn) (X.-J. Chen).

anharmonic information in candidate thermoelectrics for designing materials with low  $\kappa$  [15–17]. Meanwhile, lattice anharmonicity, which plays an important role in the process of thermal conduction in a crystal, can be directly estimated from the Grüneisen parameters [18]. So far, the Grüneisen parameters for thermoelectric materials are mainly estimated theoretical calculations, but the measurements in experimental efforts are still rare. Historically, theoretical calculations often emphasize the significance of acoustic phonons acting in thermal conductivity, but the contributions of optical phonons are always assumed to be negligible due to their relatively low group velocities and short lifetimes [19,20]. However, recently abundant works have highlighted the important contributions of optical modes on the thermal conductivity of bulk materials, especially the complex and nanoscaled structural materials [21–23]. For instance, the contributions of optical phonons remain about 25% for PbSe and 22% for PbTe between the considered temperature range (300–700 K), even through only half of the modes are optical phonons [24]. Moreover, the optical phonons can provide essential scattering channels for acoustic phonons, which are essential for the low thermal conductivity of PbSe and PbTe [25,26]. Therefore, further analyzing the anharmonic information of optical phonons is crucial for revealing the thermal transport properties in thermoelectric materials.

In this work, to investigate the thermal transport properties of the potential thermoelectric material, PdS, we firstly present the phonon dispersion and phonon density of state of PdS in terms of first-principles theory. The Raman scattering measurements are performed to study the optical phonons in PdS at high pressures. The measurements of X-ray diffraction are carried out to obtain equation of state and the bulk modulus for this material. The mode-Grüneisen parameter for each optical phonon mode is then determined by combining with Raman scattering and X-ray diffraction data. Our results not only help to understand the thermal transport behavior in PdS, but also provide a clue for understanding the phonon anharmonicity in other thermoelectric materials.

## 2. Experimental details

The detailed synthetic procedure of this high-quality sample PdS used in this experiment can be seen in elsewhere [13]. For the Raman scattering experiments, pressure was realized by using a symmetrical diamond anvil cell (DAC) with a 300  $\mu\text{m}$  culet. The sample chamber with the diameter of 150  $\mu\text{m}$  was created in a gasket (T301). A small piece of the sample (about 30  $\times$  30  $\times$  20  $\mu\text{m}^3$ ) together with a small ruby ball was loaded into the sample chamber. Then, liquid neon was loaded into the chamber as the transition medium. The power of exciting laser was 2 mW with a wavelength of 488 nm, and the integral time was 5 min in order to obtain better Raman spectra. The scattered light was focused on 1800 g/mm grating and then recorded with a 1024 pixel Princeton charge-coupled device.

For the synchrotron study, the XRD patterns were collected at the Shanghai Synchrotron Radiation Facility with the wavelength of 0.6199 Å and the size of the focus beam is less than 2  $\mu\text{m}$ . The prepared DAC was the same as that in the Raman measurements. The sample was pressed into powders before being filled in the chamber. The obtained two dimensional XRD patterns were integrated into one dimensional patterns with the help of Fit2D software [27]. The integrated intensity vs  $2\theta$  diffraction patterns were analyzed based on the Le Bail method by using the software of GSAS [28]. For all the experiments mentioned above, the pressure was calibrated by using the ruby fluorescence shift [29], and the pressure was implemented around room temperature.

## 3. AB INITIO calculation details

The density functional theory (DFT) calculations are carried out by using the Vienna ab-initio Simulation Package (VASP) [30]. The traditional Kohn-Sham Density Functional Theory are employed accompanied with the generalized gradient approximations for exchange-correlation functions [31,32]. We choose the PBEsol [33], a revised parameterization of GGA by Perdew, Burke, and Ernzerhof, for the improved description of the equilibrium properties of densely-packed solids. The electrons explicitly included in the calculations are the 4d<sup>10</sup> electrons for palladium atoms and 3s<sup>2</sup>3p<sup>4</sup> electrons for sulfur atoms. The core electrons are replaced by the projector augmented wave and pseudo-potential approach [34,35]. A plane-wave cutoff of 520 eV is used to avoid Pullay stress in geometry optimization and all the rest calculations used the plane-wave cutoff of 400 eV. The irreducible Brillouin Zone was sampled with a Gamma-centered 6  $\times$  6  $\times$  6 **k**-mesh. The Gaussian smearing was employed to determine the partial occupancies for each orbitals with smearing width of 0.01 eV. The convergence of the total energy and forces is  $1.0 \times 10^{-5}$  eV and  $1.0 \times 10^{-3}$  eV/Å, respectively. The phonon dispersion curves and thermal properties are calculated using the finite displacement method implemented in the phonopy package [36]. A super cell containing 2  $\times$  2  $\times$  2 unit cell (128 atoms in total) are used to avoid significant artificial image interactions due to finite displacement for the force constants calculations. A 21  $\times$  21  $\times$  21 *q*-mesh are used for phonon calculations. The high symmetry branches are selected according to the space group and crystal symmetry, same as those in Ref. [37].

Raman vibration modes are computed using CASTEP at PBEsol level with norm conserving pseudopotentials. The inelastic scattering of monochromatic light with collective vibrations of crystals results in the energy of incident photons being shifted depending on spatial derivatives of the macroscopic polarization [38]. The calculation of the polarization for each branch displacement is achieved by a linear response formalism [39]. The energy cutoff for the plane-wave basis is 400 eV. The irreducible Brillouin Zone was sampled with a Gamma-centered 4  $\times$  4  $\times$  4 **k**-mesh. The convergence of the total energy and forces is  $1.0 \times 10^{-5}$  eV and  $1.0 \times 10^{-2}$  eV/Å, respectively.

## 4. Results and discussion

In this section, we present the first-principles calculations based on the frame of density functional theory that can give access to the phonon dispersion and phonon density of states. These results can provide key information for the phonon anharmonicity and thus for the thermal conductivity. The results of the phonon band structure along several high symmetry lines in Brillouin zone and its corresponding density of states are shown in Fig. 1. It can be seen that no imaginary frequencies are presented among all phonon modes, which indicates that the crystal is dynamically stable. All the positive phonon modes confirm that the atomic structures are in an energy-minimum position in a configurational space. In detail, this spectra displays a bipartite structure. The upper side is coincidence with the optical modes and the lower side (red lines) is coincidence with the folded acoustic modes. For the acoustic branches, the distinctions of phonon velocities along the directions of *xx* axis ( $\Gamma - X$ ) and *zz* axis ( $\Gamma - Z$ ) are not distinct. Compared with the transverse acoustic (TA) branches, the longitudinal acoustic (LA) branch has a relatively large phonon velocity, which means that the LA branch contributes more to the total lattice thermal conductivity.

For the optical branches, a large gap of 100  $\text{cm}^{-1}$  between high frequency optical modes and the low-frequency modes can be observed. The high-frequency optical modes are mainly due to the

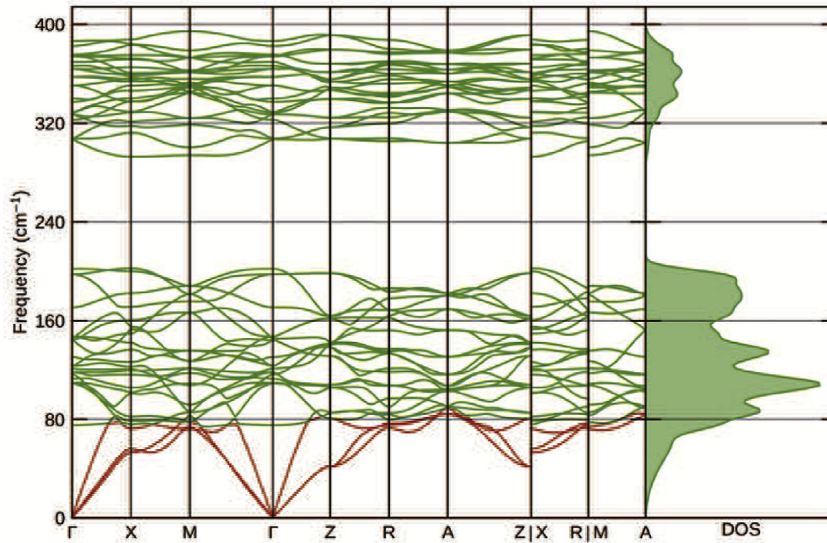


Fig. 1. Phonon dispersion (left) and phonon density of states (right) in PdS as obtained from DFT calculations.

vibrations of the S atoms, while the acoustic and low-frequency optical modes of phonon dispersions are mainly from Pd vibrations. Obviously, the low-frequency optical modes have larger dispersion than high-frequency ones, indicating that low frequency ones have relatively large group velocities, and thus have more contributions to the lattice thermal conductivity. The low-frequency optical modes and acoustic modes overlap near the frequency of  $80\text{ cm}^{-1}$ . This overlap gives a stronger evidence for the crucial of optical modes to the lattice thermal conductivity of PdS. Thus, for understanding the high thermal conductivity of PdS, it is necessary to further analysis the important role of optical modes, especially the anharmonicity of them.

Raman scattering is very useful to investigate the optical phonon branches at the Brillouin zone center. Moreover, it can provide information about point defects and intermolecular forces which are strongly related to thermal conductivity [17,40,41]. The

selected pressure dependent Raman spectra of PdS at room temperature (RT) are shown in Fig. 2 (left). A comparison Raman spectrum at 10 K and ambient pressure extracted from previous work is also shown in the left of Fig. 2 [42]. As can be seen from the Raman spectrum at 10 K, it exhibits two pronounced bands, which is consistent with the results shown in Fig. 1. They are related to the low-energy phonons ( $\sim 80\text{--}160\text{ cm}^{-1}$ ) containing five peaks and high-energy phonons ( $\sim 300\text{--}400\text{ cm}^{-1}$ ) containing seven peaks, respectively. However, only five Raman peaks can be clearly detected at RT for the high-energy phonons. It may be attributed to the very weak intensity of the missing peaks. In order to give a visualized evolution of the phonon information, the pressure-dependent phonon map is drawn up in the right of Fig. 2. With increasing pressure, both the phonon bands become broadening, obviously. These phenomena are induced by the increased phonon scattering under pressure. Furthermore, the high-energy band has

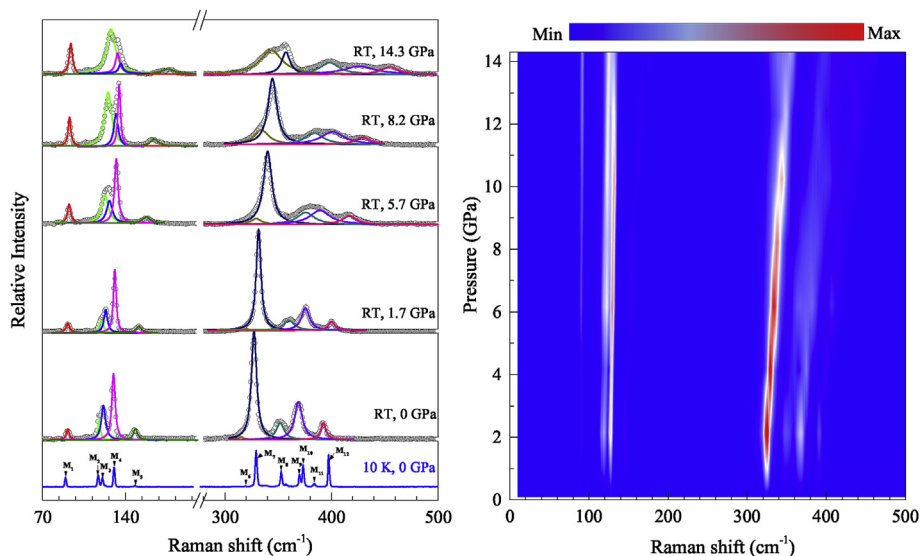
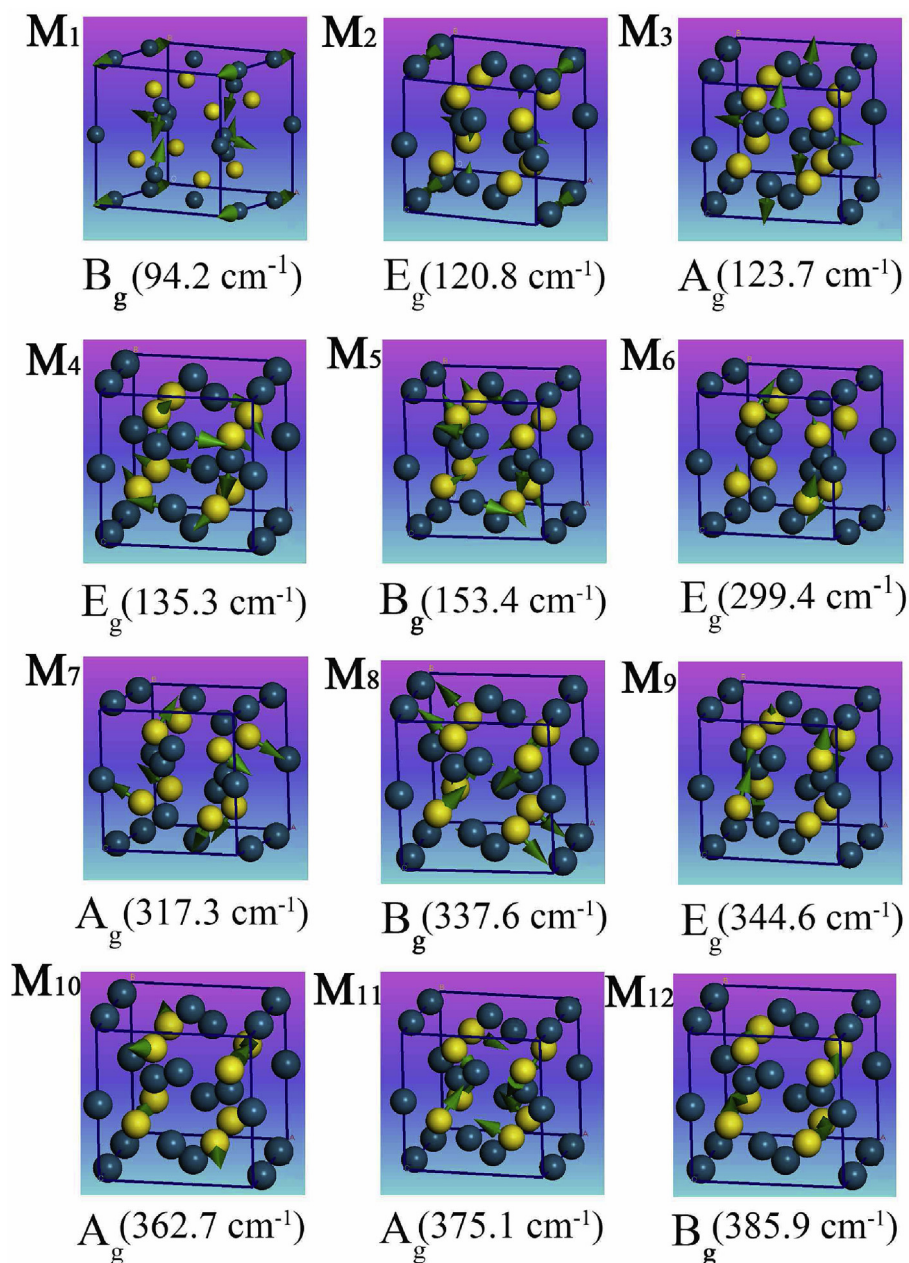


Fig. 2. Left: Selected Raman spectra of PdS at different pressures up to 14.3 GPa. The blue curve shows the Raman spectrum measured at 10 K and ambient pressure. To simplify, the Raman peaks are labelled by letters. Others experimental Raman spectra are plotted with open circles and fitted by the Lorentz function. Right: Evolution of the Raman spectra of PdS with pressure. (For interpretation of the references to colour in this figure legend, the reader is referred to the Web version of this article.)

**Table 1**

Comparison of the calculated frequencies ( $\omega_{cal}$ ) and experimental ones at temperature of 10 K ( $\omega_{10K}$ ) and room temperature ( $\omega_{RT}$ ) of selected Raman modes of PdS in the unit of  $\text{cm}^{-1}$ .

	$\omega_{cal}$	123.7	148.8	317.3	362.7	375.1					
$A_g$	$\omega_{10K}$	121.6	–	331.8	375.3	385.5					
	$\omega_{RT}$	121.2	–	326.9	368.8	–					
	Label	$M_3$	–	$M_7$	$M_{10}$	$M_{11}$					
$B_g$	$\omega_{cal}$	94.2	121.4	153.4	337.6	357.1	385.9				
	$\omega_{10K}$	89.8	–	149.8	355	–	398.8				
	$\omega_{RT}$	91.3	–	147.8	351.6	–	392.4				
$E_g$	Label	$M_1$	–	$M_5$	$M_8$	–	$M_{12}$				
	$\omega_{cal}$	120.8	121.4	135.3	148.8	299.4	299.4	322	322	344.6	344.6
	$\omega_{10K}$	118.1	–	131.8	–	321.4	–	–	–	371.9	–
	$\omega_{RT}$	117.6	–	128.8	–	314.7	–	–	–	–	–
	Label	$M_2$	–	$M_4$	–	$M_6$	–	–	–	$M_9$	–



**Fig. 3.** Calculated vibrational patterns for the Raman modes that are observed at 10 K. The vibration modes and frequencies are also shown in the bottom of each pattern.

more obvious shift and greater broadening with increasing pressure. This comparison follows that the high-energy phonons are more sensitive to pressure than the low-energy phonons in this system.

To further understand the Raman vibration modes, we perform the theory analysis. PdS has a tetragonal structure belonging to the space group  $P4_2/m$  (84) with unit cell parameters as follows:  $a = 6.440 \pm 0.005 \text{ \AA}$ ,  $c = 6.620 \pm 0.005 \text{ \AA}$  [13]. The tetragonal phase of PdS contains eight Pd atoms and eight S atoms in one unit cell. This group has 48 optical modes by theory prediction. Among them, 21 modes are Raman active ( $6B_g + 5A_g + 10E_g$ ), 19 modes are IR active ( $14E_u + 5A_u$ ) and 8 modes are inactive ( $2E_u + 1A_u + 5B_u$ ). We can only observe four modes of  $A_g$ , four modes of  $B_g$ , and four modes of  $E_g$  at 10 K with the excited laser wavelength of 488 nm. When the temperature increases to RT, some Raman peaks become very weak or even invisible. The comparison of the calculated and experimental Raman modes of PdS is summarized in Table 1. The calculated vibrational patterns for the Raman modes observed at 10 K are shown in Fig. 3. The Raman vibrational patterns are also labelled by letters, which are the same as the marked arrows in Fig. 2. Combined with the Raman spectra and Raman vibrational patterns, it can be confirmed that the relative higher energy branches pertain to predominantly sulfide-like vibrations, and the lower energy branches consist of mainly palladium-like vibrations.

The mode Grüneisen ( $\gamma_i$ ) parameters can reflect the strength of anharmonic interactions, and generally larger  $\gamma$  coupled with a strong phonon-phonon interaction induces lower lattice thermal conductivity due to strong anharmonicity [18]. Here, unlike the method of obtaining Grüneisen parameter by theoretical calculations in thermoelectrics, we provide direct measurements of the mode-Grüneisen parameters for each phonon mode observed in the Raman spectra (Fig. 2). The volume dependent change for a phonon of frequency  $\omega_i$  is characterized by the mode-Grüneisen parameter  $\gamma_i$ , defined as [43]:

$$\gamma_i = -\frac{d \ln \omega_i}{d \ln V} = \frac{B_0}{\omega_i} \frac{d \omega_i}{d P}, \quad (1)$$

where  $V$  is the unit-cell volume,  $B_0$  is the bulk modulus at ambient pressure, and  $\omega_i$  is the frequency of the phonon mode.

In order to obtain the mode-Grüneisen parameter for each phonon mode, the evolution of each phonon frequency with increasing pressure is plotted in Fig. 4. Obviously, all the phonon frequencies show upshift upon compression with no distinct deviations. The frequency of each phonon modes under pressure was fitted with a quadratic function of pressure:

$$\omega_i(P) = \omega_{i0} + \frac{d\omega_i}{dP}P - \frac{d^2\omega_i}{dP^2}P^2, \quad (2)$$

where  $\omega_{i0}$  is the phonon frequency at ambient pressure and room temperature. The fitted results are summarized in Table 2.

To obtain the  $B_0$  of PdS, the measurements of XRD were carried out. The evolution of XRD patterns with pressure of PdS at room temperature is shown in Fig. 5 (upper panel). It can be seen that all the diffraction peaks monotonically shift to higher angles with increasing pressure, showing the shrinkage of the lattice. No new diffraction peaks, peak merging and/or splitting are observed in the XRD patterns, indicating the structure of PdS is stable at high pressures up to 13 GPa. All the XRD patterns can be fitted well with a tetragonal structure belonging to the space group  $P4_2/m$  (84) through a typical Le Bail fitting. A selected fitted XRD pattern based on tetragonal structure model at the pressure of 1.2 GPa is shown in the lower panel (Fig. 5). The fitting yields reasonable factors of  $R_p = 3.4\%$ ,  $R_{wp} = 4.8\%$ , and  $\chi^2 = 3.1\%$ . The lattice parameters at this

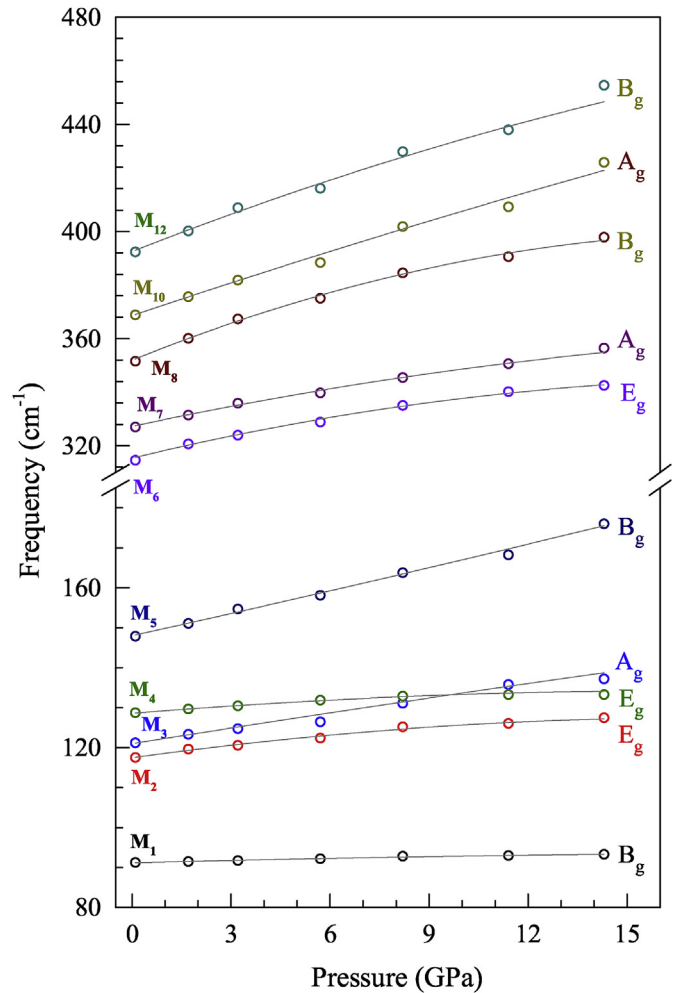


Fig. 4. Pressure dependence of the phonon frequencies of selected modes for PdS at room temperature. The solid curves are the polynomial fittings to the experimental data points.

pressure are  $a = 6.359 \pm 0.009 \text{ \AA}$ ,  $c = 6.536 \pm 0.009 \text{ \AA}$ .

Depending on the refined results of the XRD patterns, the pressure dependence of the lattice parameters along the  $a$  and  $c$  axes,  $V$ , and the corresponding axial ratio  $a/c$ , are shown in Fig. 6, respectively. According to the expected equation of state, both the lattice parameters and volume have no obvious deviation to the applied pressure within experimental errors. Depending on the Murnaghan equation of state [44],

$$P = \frac{3B_0}{2} \left[ \left( \frac{V}{V_0} \right)^{7/3} \right] \left\{ 1 + \frac{3}{4} (B'_0 - 4) \left[ \left( \frac{V}{V_0} \right)^{2/3} - 1 \right] \right\}, \quad (3)$$

where  $V_0$  is the unit-cell volume at ambient pressure. Hence, we obtain the bulk modulus  $B_0$  of  $98.5 \pm 3.6 \text{ GPa}$  for PdS. It is an essential parameter for calculating the mode-Grüneisen parameter for each phonon mode. Notably, pressure-induced lattice variation can give an index to the distortion in crystal. As shown in the inset of Fig. 6(b), the ratio  $a/c$  firstly remains the same with increasing pressure until about 4 GPa, then it has a continuous increase upon further compression.

Combining Eqs. (1) and (2) together with the value of  $B_0$ , we can obtain the mode-Grüneisen parameters from experiments. The values of  $\gamma_i$  for each phonon mode are also summarized in Table 2. These values give a new insight into the understanding of the

**Table 2**

Summary of the vibrational modes, frequencies  $\omega_{j0}$  ( $\text{cm}^{-1}$ ), their pressure coefficients  $\frac{d\omega_j}{dP}$  ( $\text{cm}^{-1}/\text{GPa}$ ) and  $\frac{d^2\omega_j}{dP^2}$  ( $\times 10^{-2} \text{ cm}^{-1}/\text{GPa}^2$ ), and the mode-Grüneisen parameters  $\gamma_i$ 's for each phonon mode observed in PdS.

Label	M <sub>1</sub> (B <sub>g</sub> )	M <sub>2</sub> (E <sub>g</sub> )	M <sub>3</sub> (A <sub>g</sub> )	M <sub>4</sub> (E <sub>g</sub> )	M <sub>5</sub> (B <sub>g</sub> )	M <sub>6</sub> (E <sub>g</sub> )	M <sub>7</sub> (A <sub>g</sub> )	M <sub>8</sub> (B <sub>g</sub> )	M <sub>10</sub> (A <sub>g</sub> )	M <sub>12</sub> (B <sub>g</sub> )
$\omega_{j0}$	91.2	117.5	121	128.5	148	315.3	327.3	351.9	368.6	392.4
$\frac{d\omega_j}{dP}$	0.21 ± 0.04	1.14 ± 0.14	1.31 ± 0.12	0.67 ± 0.05	1.83 ± 0.25	2.97 ± 0.27	2.63 ± 0.34	4.98 ± 0.40	4.14 ± 0.32	4.25 ± 0.70
$\frac{d^2\omega_j}{dP^2}$	0.41 ± 0.22	3.25 ± 0.96	0.50 ± 0.97	2.02 ± 0.56	0.64 ± 0.71	7.42 ± 1.61	4.88 ± 2.87	13.01 ± 2.75	2.42 ± 2.78	0.01 ± 0.00
$\gamma_i$	0.23 ± 0.02	0.91 ± 0.09	0.83 ± 0.07	0.49 ± 0.03	1.12 ± 0.15	0.87 ± 0.08	0.78 ± 0.10	1.32 ± 0.10	1.05 ± 0.08	1.06 ± 0.15

phonon anharmonicity in this system. As mentioned above, large  $\gamma$  value means strong lattice anharmonicity. Thus, the phonon mode B<sub>g</sub> at  $352 \text{ cm}^{-1}$  with  $\gamma_{B_g} = 1.32$  and the phonon mode B<sub>g</sub> at  $148 \text{ cm}^{-1}$  with  $\gamma_{B_g} = 1.12$  likely play prominent roles in the procedure of phonon scattering, because of their relative larger values. The two larger  $\gamma$ 's give the fact that the phonon scattering in this system is mainly induced by the combined effects of Pd atoms and S atoms. The different values of the mode-Grüneisen parameters illustrate the disparate contribution of the observed phonon modes to the phonon anharmonicity. For the low-energy phonons potentially coupled with acoustic phonons, the mode-Grüneisen parameters of them are very small. This phenomenon may provide a clue for understanding the high thermal conductivity of PdS. In addition, we further calculate the average Grüneisen parameter of

each phonon mode by using the formula of [45]  $\bar{\gamma} = \sqrt{\langle \gamma_i^2 \rangle}$ . The calculated value of  $\bar{\gamma}$  is about 0.9. However, this value is still very small compared with the theoretical calculated value of typical thermoelectric materials, such as SnSe ( $\gamma = 4.1$  along the *a* axis) and AgSbSe<sub>2</sub> ( $\gamma = 3.5$ ) [18,46]. The small average Grüneisen parameter also gives an index to the high thermal conductivity of PdS at high temperatures. Thus, increasing phonon anharmonicity which contributes to the complex phonon density of states in crystal, may be an effective way to reduce the lattice thermal conductivity.

This information from the mode-Grüneisen parameter gives an index that increasing the phonon anharmonicity may be very important and useful for reducing the thermal conductivity at high temperatures. Many methods have been proposed to reduce

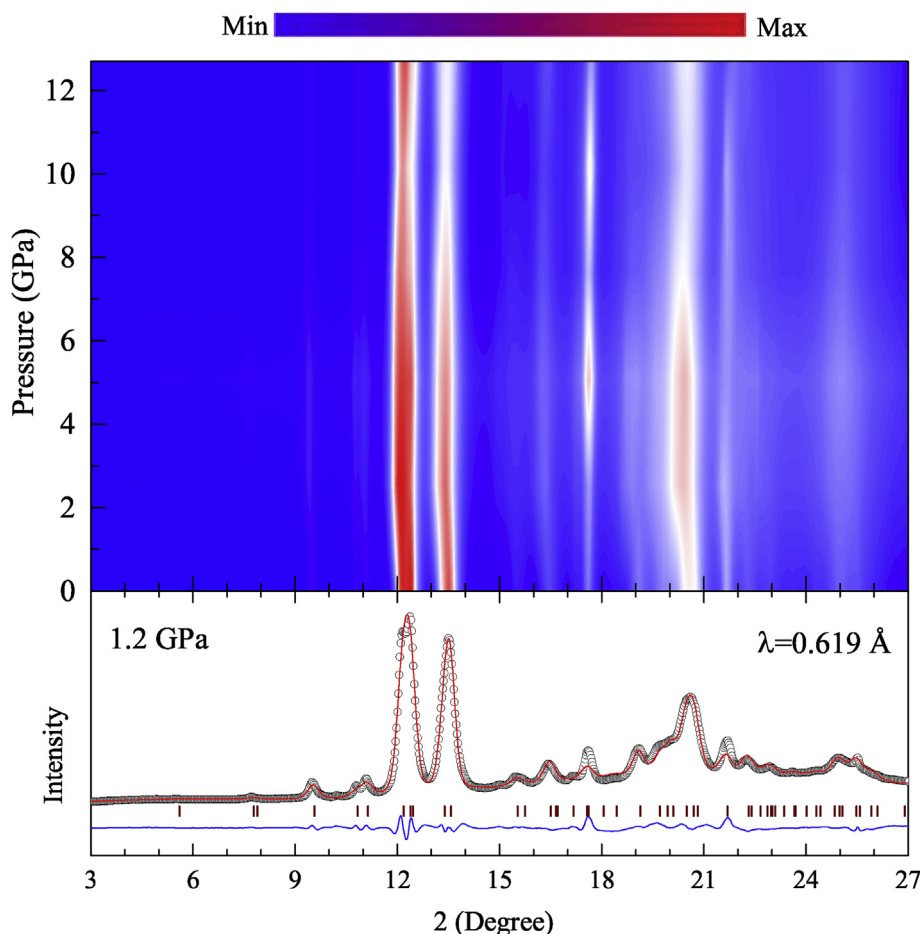


**Fig. 5.** The integrated powder X-ray diffraction data of PdS at various pressures up to 13 GPa (upper panel). The lower panel shows the selected X-ray diffraction pattern at the pressure of 1.2 GPa. The upper continuous red line is the fitted result, and the difference between the observed and calculated profiles (bottom blue line) is obtained after Le Bail fitting for the sample at 1.2 GPa. The middle sticks refer to the peak positions. (For interpretation of the references to colour in this figure legend, the reader is referred to the Web version of this article.)

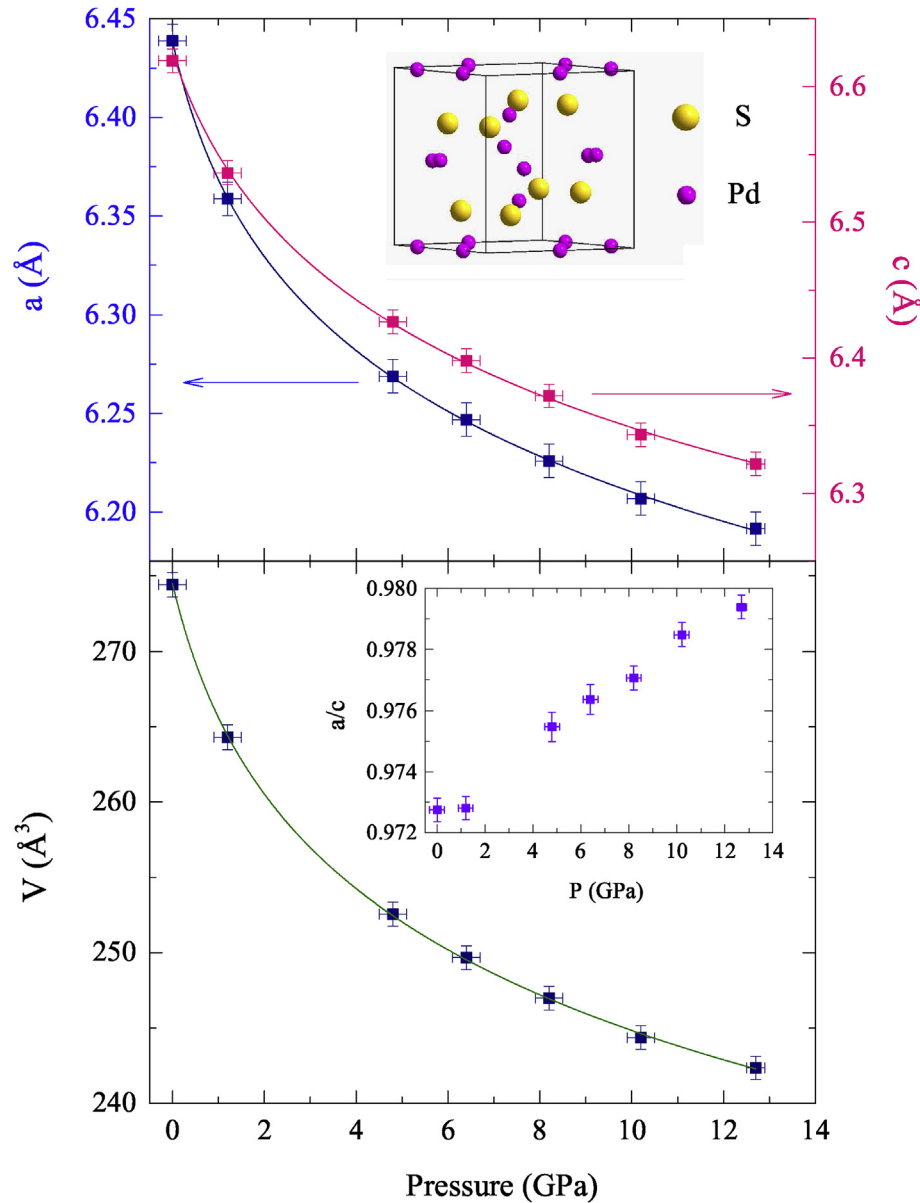


**Fig. 6.** The lattice parameters along the  $a$  and  $c$  axes (a) and the unit-cell volume  $V$  (b) of PdS as a function of pressure up to 13 GPa. The solid points are the measured data and the curves are the fitting results of the Murnaghan equation of state. The inset of (a) illustrates the crystal structure of PdS. The inset of (b) presents the pressure dependence of the axial ratio  $a/c$ .

thermal conductivity, such as doping, alloying, nanostructuring, and all-scale structures [1–6]. More importantly, we have found that applying pressure is very effective in turning the thermal conductivity [14,47]. In order to provide a further understanding about the evolution of thermal conductivity with pressure, we now take a closer look at the pressure-dependent full width at half maximum (FWHM) of the phonon mode.

The FWHMs of Raman peaks can be used to investigate the procedure of phonon scattering, because of their associated relationship with the phonon mean free path [48–50]. Fig. 7 shows the pressure dependence of FWHMs of the selected Raman peaks from ambient pressure to 14.3 GPa. The last panel of Fig. 7 shows the pressure dependence of  $\kappa$  for PdS around RT (adapted from Ref. 11). The phonon modes of  $E_g$  at  $128.8\text{ cm}^{-1}$ ,  $A_g$  at  $326.9\text{ cm}^{-1}$ , and  $A_g$  at  $368.8\text{ cm}^{-1}$  are selected as examples to illustrate, because of their relatively good peak shapes and intensities. The FWHMs were

extracted from the experimental Raman spectra of PdS, fitted by Lorentzian function. As can be seen, the FWHM of each selected phonon mode has an obvious broadening tendency with increasing pressure up to 4 GPa, and then the phonon mode saturates upon further compression. The phonon lifetime ( $\tau_i$ ), which is positively related to the thermal conductivity, can be obtained through the damped harmonic oscillator model of Lorentz with the expression [51,52]:

$$\tau_i = \frac{1}{2\pi\text{FWHM}_i} \quad (4)$$

Thus, the evolution of the FWHMs with pressure is consistent with the pressure dependence of the thermal conductivity in PdS. Meanwhile, the self-consistent evolution of the FWHMs and thermal conductivity illustrates the important components of the optical phonons to the thermal transports of PdS. In addition, the

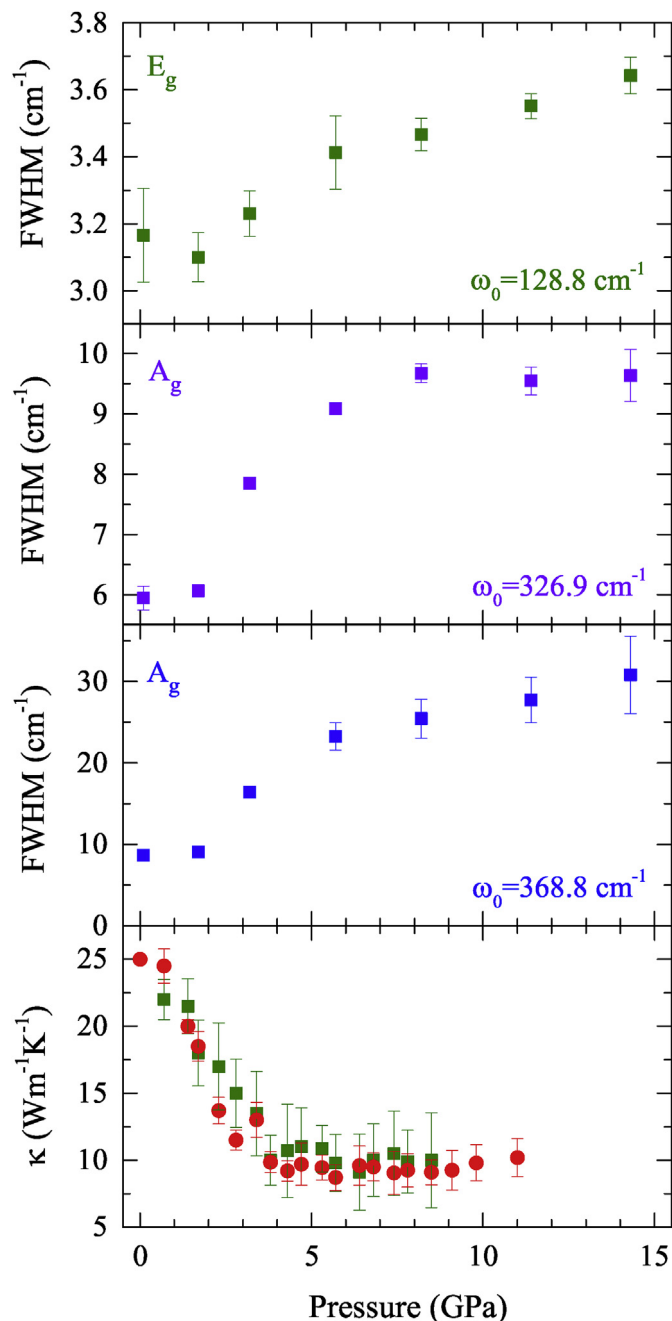


**Fig. 7.** Representative pressure dependent linewidths in the full width at half maxima (FWHMs) of the phonon modes ( $E_g$  at  $128.8\text{ cm}^{-1}$ ,  $A_g$  at  $326.9\text{ cm}^{-1}$ , and  $A_g$  at  $368.8\text{ cm}^{-1}$ , respectively) of PdS at room temperature. The last panel shows the pressure dependence of  $\kappa$  for PdS around RT (adapted from Ref. 11).

decreased lattice parameters and the discontinuous ratio  $a/c$  under pressure have also provided suggested reasons for the decreased thermal conductivity of PdS at low pressures.

## 5. Conclusions

In summary, we have calculated the phonon dispersion and related phonon density of states of a potential thermoelectric compound PdS. The phonon dispersion revealed the important contributions of optical phonon modes to the lattice thermal conductivity for this material. We also have performed the Raman

scattering and X-ray diffraction measurements at pressures up to 14 GPa in order to obtain the optical phonon spectra and the evolution of the structure with pressure. The observed optical phonon modes in Raman spectra have been firstly assigned through theoretical calculations. The tetragonal structure of PdS is found to be stable in the studied pressure range. The bulk modulus of PdS at ambient pressure was obtained through the experimentally determined structural data. Combining with the fitted results of the optical phonon frequencies, we obtained the mode-Grüneisen parameter for each optical phonon mode. The small mode-Grüneisen given a reasonable explanation for the high thermal conductivity of PdS at ambient pressure. In addition, the lattice ratio  $a/c$  and FWHMs of Raman peaks under pressure are consistent with evolution of the thermal conductivity with pressure. These phenomena give a further understanding about the decrease of thermal conductivity in PdS upon compression.

## Acknowledgments

Xun Shi and Li-Dong Chen acknowledged the support from the National Natural Science Foundation of China under the No. 51625205, the Key Research Program of Chinese Academy of Sciences (Grant No. KFZD-SW-421), and the Program of Shanghai Subject Chief Scientist (16XD1403900). Lei Su acknowledged the support from the National Natural Science Foundation of China (No. 21273206).

## References

- [1] G. Chen, M. Dresselhaus, G. Dresselhaus, J.-P. Fleurial, T. Caillat, Recent developments in thermoelectric materials, *Int. Mater. Rev.* 48 (2003) 45–66.
- [2] Z. Ren, Y. Lan, Q. Zhang, *Advanced Thermoelectrics: Materials, Contacts, Devices, and Systems*, CRC Press, 2017.
- [3] X. Shi, L. Chen, C. Uher, Recent advances in high-performance bulk thermoelectric materials, *Int. Mater. Rev.* 61 (2016) 379–415.
- [4] G.J. Snyder, E.S. Toberer, Complex thermoelectric materials, *Nat. Mater.* 7 (2008) 105–114.
- [5] L.E. Bell, Cooling, heating, generating power, and recovering waste heat with thermoelectric systems, *Science* 321 (2008) 1457–1461.
- [6] X. Shi, L. Chen, Thermoelectric materials step up, *Nat. Mater.* 15 (2016) 691–692.
- [7] J. Folmer, J. Turner, B. Parkinson, Photoelectrochemical characterization of several semiconducting compounds of palladium with sulfur and/or phosphorus, *J. Solid State Chem.* 68 (1987) 28–37.
- [8] I. Ferrer, P. Díaz-Chao, A. Pascual, C. Sánchez, An investigation on palladium sulphide (PdS) thin films as a photovoltaic material, *Thin Solid Films* 515 (2007) 5783–5786.
- [9] M. Barawi, I. Ferrer, J. Ares, C. Sánchez, Hydrogen evolution using palladium sulphide (PdS) nanocorals as photoanodes in aqueous solution, *ACS Appl. Mater. Interfaces* 6 (2014) 20544–20549.
- [10] C. Yang, Y. Wang, C. Wan, C. Chen, A search for the mechanism of direct copper plating via bridging ligands, *J. Electrochem. Soc.* 143 (1996) 3521–3525.
- [11] J.J. Bladon, A. Lamola, F.W. Lytle, W. Sonnenberg, J.N. Robinson, G. Philipose, A palladium sulfide catalyst for electrolytic plating, *J. Electrochem. Soc.* 143 (1996) 1206–1213.
- [12] L.-C. Chen, H. Yu, H.-J. Pang, B.-B. Jiang, L. Su, X. Shi, L.-D. Chen, X.-J. Chen, Pressure-induced superconductivity in palladium sulfide, *J. Phys. Condens. Matter* 30 (2018) 155703.
- [13] L.-C. Chen, B.-B. Jiang, H. Yu, H.-J. Pang, L. Su, X. Shi, L.-D. Chen, X.-J. Chen, Thermoelectric properties of polycrystalline palladium sulfide, *RSC Adv.* 8 (2018) 13154–13158.
- [14] L.-C. Chen, H. Yu, H.-J. Pang, B.-B. Jiang, L. Su, X. Shi, L.-D. Chen, X.-J. Chen, Pressure-induced enhancement of thermoelectric performance in palladium sulfide, *Mater. Today Phys.* 5 (2018) 64–71.
- [15] Y. Zhang, E. Skoug, J. Cain, V. Ozoliņš, D. Morelli, C. Wolverton, First-principles description of anomalously low lattice thermal conductivity in thermoelectric Cu-Sb-Te ternary semiconductors, *Phys. Rev. B* 85 (2012), 054306.
- [16] D. Bessas, I. Sergueev, H.-C. Wille, J. Perlfson, D. Ebling, R. Hermann, Lattice dynamics in  $\text{Bi}_2\text{Te}_3$  and  $\text{Sb}_2\text{Te}_3$ : Te and Sb density of phonon states, *Phys. Rev. B* 86 (2012) 224301.
- [17] O. Delaire, A.F. May, M.A. McGuire, W.D. Porter, M.S. Lucas, M.B. Stone, D.L. Abernathy, V. Ravi, S. Firdosy, G. Snyder, Phonon density of states and heat capacity of  $\text{La}_{3-x}\text{Te}_4$ , *Phys. Rev. B* 80 (2009) 184302.
- [18] L.-D. Zhao, S.-H. Lo, Y. Zhang, H. Sun, G. Tan, C. Uher, C. Wolverton, V.P. Dravid, M.G. Kanatzidis, Ultralow thermal conductivity and high thermoelectric figure

- of merit in SnSe crystals, *Nature* 508 (2014) 373–377.
- [19] G. Srivastava, Phonon conductivity of insulators and semiconductors, *J. Phys. Chem. Solids* 41 (1980) 357–368.
- [20] G. Chen, Thermal conductivity and ballistic-phonon transport in the cross-plane direction of superlattices, *Phys. Rev. B* 57 (1998) 14958.
- [21] A. Giri, P.E. Hopkins, Role of interfacial mode coupling of optical phonons on thermal boundary conductance, *Sci. Rep.* 7 (2017) 11011.
- [22] Z. Tian, K. Esfarjani, J. Shiomi, A.S. Henry, G. Chen, On the importance of optical phonons to thermal conductivity in nanostructures, *Appl. Phys. Lett.* 99 (2011), 053122.
- [23] A. Greenstein, Y. Hudiono, S. Graham, S. Nair, Effects of nonframework metal cations and phonon scattering mechanisms on the thermal transport properties of polycrystalline zeolite LTA films, *J. Appl. Phys.* 107 (2010), 063518.
- [24] Z. Tian, J. Garg, K. Esfarjani, T. Shiga, J. Shiomi, G. Chen, Phonon conduction in PbSe, PbTe, and  $\text{PbTe}_{1-x}\text{Se}_x$  from first-principles calculations, *Phys. Rev. B* 85 (2012) 184303.
- [25] Y. Zhang, X. Ke, C. Chen, J. Yang, P. Kent, Thermodynamic properties of PbTe, PbSe, and PbS: first-principles study, *Phys. Rev. B* 80 (2009), 024304.
- [26] O. Delaire, J. Ma, K. Marty, A.F. May, M.A. McGuire, M.-H. Du, D.J. Singh, A. Podlesnyak, G. Ehlers, M. Lumsden, et al., Giant anharmonic phonon scattering in PbTe, *Nat. Mater.* 10 (2011) 614–619.
- [27] A. Hammersley, S. Svensson, M. Hanfland, A. Fitch, D. Hausermann, Two-dimensional detector software: from real detector to idealised image or two-theta scan, *Int. J. High Pressure Res.* 14 (1996) 235–248.
- [28] B.H. Toby, XPGUI, a graphical user interface for GSAS, *J. Appl. Crystallogr.* 34 (2001) 210–213.
- [29] H. Mao, P. Bell, J. t. Shaner, D. Steinberg, Specific volume measurements of Cu, Mo, Pd, and Ag and calibration of the ruby R1 fluorescence pressure gauge from 0.06 to 1 Mbar, *J. Appl. Phys.* 49 (1978) 3276–3283.
- [30] G. Kresse, J. Hafner, Ab initio molecular dynamics for liquid metals, *Phys. Rev. B* 47 (1993) 558.
- [31] P. Hohenberg, W. Kohn, Inhomogeneous electron gas, *Phys. Rev.* 136 (1964) B864.
- [32] W. Kohn, L.J. Sham, Self-consistent equations including exchange and correlation effects, *Phys. Rev.* 140 (1965) A1133.
- [33] J.P. Perdew, A. Ruzsinszky, G.I. Csonka, O.A. Vydrov, G.E. Scuseria, L.A. Constantin, X. Zhou, K. Burke, Restoring the density-gradient expansion for exchange in solids and surfaces, *Phys. Rev. Lett.* 100 (2008) 136406.
- [34] P. Blöchl, Projector augmented-wave method, *Phys. Rev. B* 50 (1994) 17953.
- [35] R.O. Jones, O. Gunnarsson, The density functional formalism, its applications and prospects, *Rev. Mod. Phys.* 61 (1989) 689.
- [36] A. Togo, I. Tanaka, First principles phonon calculations in materials science, *Scripta Mater.* 108 (2015) 1–5.
- [37] W. Setyawan, S. Curtarolo, High-throughput electronic band structure calculations: challenges and tools, *Comput. Mater. Sci.* 49 (2010) 299–312.
- [38] D. Porezag, M.R. Pederson, Infrared intensities and Raman-scattering activities within density-functional theory, *Phys. Rev. B* 54 (1996) 7830.
- [39] S. Baroni, S. De Gironcoli, A. Dal Corso, P. Giannozzi, Phonons and related crystal properties from density-functional perturbation theory, *Rev. Mod. Phys.* 73 (2001) 515.
- [40] D. Li, X. Qin, Y. Gu, The effects of bismuth intercalation on structure and thermal conductivity of TiS, *Mater. Res. Bull.* 41 (2006) 282–290, 2.
- [41] H.-K. Lee, D.K. Kim, Investigation on thermal conductivity of aluminum nitride ceramics by FT-Raman spectroscopy, *J. Am. Ceram. Soc.* 93 (2010) 2167–2170.
- [42] L.-C. Chen, Z.-Y. Cao, H. Yu, B.-B. Jiang, L. Su, X. Shi, L.-D. Chen, X.-J. Chen, Phonon anharmonicity in thermoelectric palladium sulfide by Raman spectroscopy, *Appl. Phys. Lett.* 113 (2018), 022105.
- [43] E. Liarokapis, E. Anastassakis, G. Kourouklis, Raman study of phonon anharmonicity in LaF, *Phys. Rev. B* 32 (1985) 8346, 3.
- [44] F. Birch, Finite elastic strain of cubic crystals, *Phys. Rev.* 71 (1947) 809.
- [45] D. Morelli, J. Heremans, G. Slack, Estimation of the isotope effect on the lattice thermal conductivity of group IV and group III-V semiconductors, *Phys. Rev. B* 66 (2002) 195304.
- [46] M.D. Nielsen, V. Ozolins, J.P. Heremans, Lone pair electrons minimize lattice thermal conductivity, *Energy Environ. Sci.* 6 (2013) 570–578.
- [47] H. Yu, L.-C. Chen, H.-J. Pang, X.-Y. Qin, P.-F. Qiu, X. Shi, L.-D. Chen, X.-J. Chen, Large enhancement of thermoelectric performance in  $\text{CuInTe}_2$  upon compression, *Mater. Today Phys.* 5 (2018) 1–6.
- [48] C. Ulrich, A. Göbel, K. Syassen, M. Cardona, Pressure-induced disappearance of the Raman anomaly in CuCl, *Phys. Rev. Lett.* 82 (1999) 351.
- [49] G. Lucazeau, Effect of pressure and temperature on Raman spectra of solids: anharmonicity, *J. Raman Spectrosc.* 34 (2003) 478–496.
- [50] Y. Tian, S. Jia, R. Cava, R. Zhong, J. Schneeloch, G. Gu, K.S. Burch, Understanding the evolution of anomalous anharmonicity in  $\text{Bi}_2\text{Te}_{3-x}\text{Se}_x$ , *Phys. Rev. B* 95 (2017), 094104.
- [51] A. Hofmeister, Mantle values of thermal conductivity and the geotherm from phonon lifetimes, *Science* 283 (1999) 1699–1706.
- [52] A.M. Hofmeister, Pressure dependence of thermal transport properties, *Proc. Natl. Acad. Sci. Unit. States Am.* 104 (2007) 9192–9197.